

Part II Applied Physics

Section 1 Atomic, Molecular and Optical Physics

Section 2 Plasma Physics

Section 3 Electromagnetics

Section 4 Radio Astronomy

RILE

*Celebrating
50 Years*

1946-1996

OF IMPACT & INNOVATION

Section 1 Atomic, Molecular and Optical Physics

Chapter 1 Quantum Optics and Photonics

Chapter 2 Basic Atomic Physics

Chapter 1. Quantum Optics and Photonics

Academic and Research Staff

Professor Shaoul Ezekiel, Dr. Selim M. Shahriar, Dr. Stephen P. Smith, Dr. Timothy Grove, Dr. Venkatapuram S. Sudarshanam

Visiting Scientists and Research Affiliates

Dr. Philip R. Hemmer,¹ Dr. Mara G. Prentiss,² John D. Kierstead¹

Graduate Students

John J. Donoghue,³ Daniel P. Katz,⁴ Juliet Mervis⁴

1.1 Classical and Quantum Noise Suppression in Distortion-Free Phase Conjugation Using Coherent Population Trapping

Sponsor

U.S. Air Force - Electronic Systems Division
Contract F19628-92-K-0013

We have observed greater than 10 dB classical noise correlations and indirect evidence of equally strong quantum noise suppression using distortion-free, four-wave mixing in optically dense sodium vapor under conditions of high gain (up to 50). To achieve such a performance in a strongly absorbing medium, it is necessary to suppress unwanted absorption effects while enhancing index modulation. We accomplish this via a process analogous to coherent population trapping (or electromagnetically induced transparency) in a pseudo-four-level, closed-loop system. This type of quantum noise suppression may be useful for broadband image squeezing in optical computers.

Four-wave mixing (FWM) has numerous potential applications to image processing, aberration correction and amplification. In addition, FWM is a natural choice for the generation of spatially broadband squeezed light for sub-shot noise

imaging applications. In general, however, these applications require a FWM mechanism that can deliver high gain without propagation distortion or excessive scattered light generation. Moreover, for sub-shot noise imaging applications, the FWM should be optimized for low intensity cw signals.

Recently, electromagnetically induced transparency (EIT) was shown to eliminate propagation distortion and even self-focusing via coherent population trapping (CPT) in optically dense media.⁵ Noise correlation via CPT has also been studied, and strong classical noise correlations observed. In a previous paper, we demonstrated high gain at low pump intensity in optically dense sodium vapor using FWM and CPT in a pseudo-double- Λ system (i.e., a three- or four-level system, excited by four fields in a closed-loop geometry, as shown in figure 1).⁶ Here, we report noise suppressions and signal propagation effects in this novel pseudo-double- Λ system.

Figure 1 shows the basic excitation scheme as well as the atomic configuration for realizing FWM via CPT in a pseudo-double- Λ system. As shown, the forward and backward pump beams, F and B respectively, excite opposite legs of separate Λ -subsystems. The input probe beam, P, completes the subsystem excited by F, and the conjugate beam, C, completes the other, as shown.

¹ Rome Laboratory, Hanscom Air Force Base, Bedford, Massachusetts.

² Professor, Department of Physics, Harvard University, Cambridge, Massachusetts.

³ Electro-optics Center, Tufts University, Medford, Massachusetts.

⁴ Department of Physics, Harvard University, Cambridge, Massachusetts.

⁵ M. Jain, A.J. Merriam, A. Kasapi, G.Y. Yin, and S.E. Harris, *Phys. Rev. Lett.* 75: 4385 (1995).

⁶ P.R. Hemmer, D.P. Katz, J. Donoghue, M. Cronin-Golomb, M.S. Shahriar, and P. Kumar, *Opt. Lett.* 20: 982 (1995).

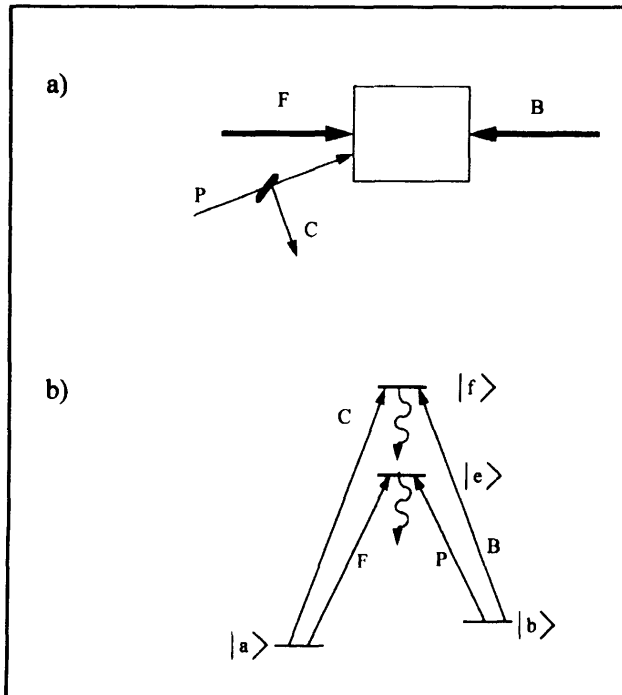


Figure 1. (a) basic-four wave mixing scheme where F is the forward pump, B is the backward pump, P is the input probe beam, and C is the conjugate. (b) double lambda atomic system with lasers F, B, P, and C.

In analogy to EIT,⁷ it is possible to view FWM in this system as a two-step process. In the first step, F and P write a grating in the ground state coherences via CPT. In the second step, beam B diffracts off this grating to produce C. This simple picture is valid in the limit of weak B and C. However, for applications, it is more realistic for the pumps F and B to be strong with P and C initially weak. In this case, it is clear that conventional CPT or EIT is not possible, since the two Λ subsystems have conflicting transparency conditions. Nonetheless, it is still possible to interpret the pseudo-double- Λ system in terms of CPT concepts by considering the four-level closed-loop transparency condition.

The transparency condition for a closed-loop, double- Λ system is more restrictive than in a single- Λ system. In addition to the requirement for properly phased atomic ground states, there are also restrictions on the relative phases and magnitudes of the four fields. The FWM geometry, shown in figure 1, automatically satisfies the phase constraint. However, the field magnitude condition is not satisfied in general. This condition requires a

relation between Rabi frequency ratios $F/P = C/B$, and is clearly far from being satisfied when P and C are weak. Still, it is possible to understand the evolution of this system in analogy with CPT. Recall that in the case of a single- Λ system an arbitrary initial atomic state can be written as a superposition of a dark state and a set of bright states. CPT causes the system to evolve into the dark state by decay. Similarly, in the double- Λ system, an arbitrary configuration of atomic and field states can be expressed as a linear combination of a closed loop dark state (for which $F/P = C/B$) and one or more bright states. Again the tendency is to evolve toward the transparent state. However, in the closed loop system, this will involve the rearrangement of both atomic and field populations (i.e., there will be optical loss and/or gain).

For example, if F and B are strong and P and C are weak, then, for opportune choices of parameters, transparency may be approached most rapidly by attenuation of F and B and gain in P and C. In addition, if F and B have initially similar strengths, it is reasonable to expect nearly equal amounts of energy to be transferred into both P and C, resulting in noise correlations. Finally, as the transparency condition is approached, the resonant nonlinear refractive index is expected to be suppressed, thereby reducing self-focusing and other propagation aberrations as in EIT.

Of course, the physical explanation just given is an oversimplification. For example, in cw FWM using the counter-propagating geometry shown in figure 1, the transparency condition is only approximately approached near the center of the cell. In this case, the nonlinear refractive index suppression is probably not mediated by EIT. Rather, experimental observations suggest that the refractive index may be controlled by canceling the nonlinear refractive index changes by spatially varying two-photon Stark shifts. These Stark shifts can produce nonlinear refractive index changes of either sign via steep refractive index variations in the neighborhood of the two-photon Raman resonance.

Figure 2 illustrates typical experimental conditions. The $3^2S_{1/2}$ ground state (hyperfine $F=1$ and $F=2$) and the $3^2P_{1/2}$ hyperfine levels ($F=1$ and $F=2$) compose the sodium system used in this report. Two dye lasers tuned near the D1 line provide the F and B beams (FWHM approximately 1.4 mm and 100 mW power). The two pumps have nearly identical beam diameters and are collimated to within 1

⁷ S.E. Harris, *Phys. Rev. Lett.* 70: 552 (1993); S.E. Harris, *Phys. Rev. Lett.* 72: 52 (1994); S.E. Harris, J.E. Field, and A. Kasapi, *Phys. Rev. A* 46: R29 (1992).

mrad. To generate the weak probe beam, P, an acousto-optical modulator shifts the frequency of a small portion of the F beam by -1.77 GHz (as shown in figure 2). This probe beam has a FWHM of approximately 0.9 mm and 1 mW of power. Figure 2 shows the typical detuning of each beam. The angles between the F and P (and B and C) are kept below 4 mrad in order to maintain a good beam overlap in the sodium cell. The sodium cell is a heat pipe oven at approximately 180° C. At this temperature, the sodium density is high enough that the near-resonant probe beam absorption is greater than 95 percent (when blocking both pump beams). Photodiodes and/or video cameras, marked as detectors in figure 2, measure the power and/or beam profiles of beams exiting the sodium cell.

Figure 3 shows the measured probe beam profiles exiting the cell. In particular, figure 3a shows the

profile for an unamplified probe (frequency tuned outside the Doppler profile). This beam is slightly larger than the 0.9 mm FWHM in the cell (the beam diffracts over the 1.2 m distance from cell to camera). Figure 3b shows an amplified probe cross section for a probe power gain of 10. The smaller FWHM diameter in this case is probably due to slight residual self focusing and is noticeable only because of the large cell to camera distance. Figure 3c illustrates the case of gain of 50, showing the onset of distortion effects. Such distortion becomes more severe for gains in excess of 100 (the largest observed gain is in excess of 1000). In both figures 3b and 3c, pump depletion effects are significant. In fact, higher gain is achieved by attenuation of the input probe power (10 dB in figure 3c).

The four-wave mixing process in the pseudo-double- Λ system is expected to yield quantum

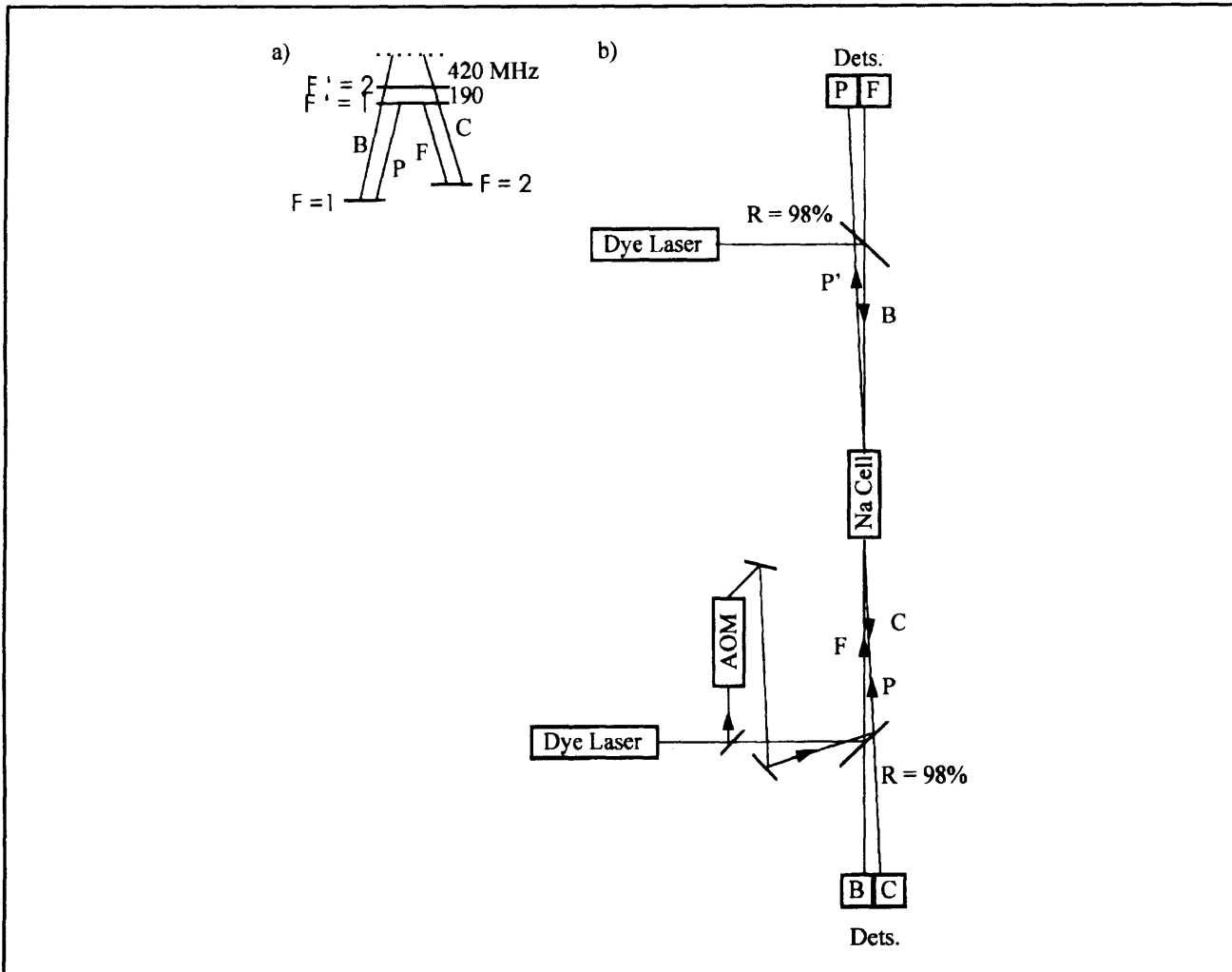


Figure 2. (a) Experimental double lambda system. Ground states consist of the $3^2S_{1/2}$ levels $F=1$ and $F=2$. Excited states consist of the $3^2P_{1/2}$ levels $F=1$ and $F=2$. Approximate detunings are given. (b) Experimental set-up showing the generation of each beam.

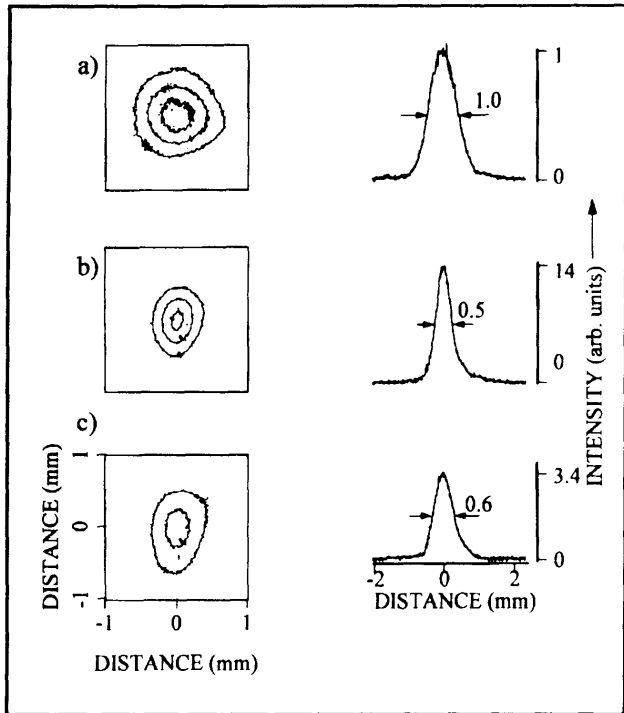


Figure 3. Contour and horizontal profiles of the probe beam and the amplified probe beam under various conditions. a) Unamplified probe, b) gain=10 amplified probe, c) gain=50 amplified probe.

noise suppression. In particular, we have shown⁸ that the conjugate and amplified probe are twin beams, with noise correlations substantially (> 10 dB) below the shot-noise limit, as illustrated in figure 4. Figure 4a shows the degree of twin beam squeezing as a function of the probe/conjugate detuning. For the case of 10 dB squeezing, the probe and conjugate are almost 10 dB quantum noise correlated (i.e., twin beams), and the correlation is illustrated using numerically computed joint photon probability distribution in figure 4b.

This correlation can be observed in the current difference of a photodiode detecting the amplified probe, and another photodiode detecting the conjugate. As usual, the calculation assumes that quantum noise of the pumps can be ignored. In addition, the two pumps (F and B) are assumed to be generated from the same laser, so that any classical noise (i.e., fluctuation in the mean intensity) is not expected to affect the probe-conjugate quantum noise correlation to first order.

However, in our experiment, two independent lasers generate the two pump beams, so that the classical noises in F and B are uncorrelated. Such a situation is extremely difficult to take into account in quantum noise correlation calculations. Nonetheless, it is possible to estimate the effects of the uncorrelated classical noises of the pump beams. Assuming ideal wave mixing (i.e., loss free), it is well known that the degree of quantum noise correlation is proportional to the gain of the probe beam.⁹ By a classical noise analysis, it is easy to show that the same conclusion applies to the classical noise correlation between the conjugate and the amplified probe in the presence of classical pump noise.

Figure 5 shows the measured intensity noise correlations between the amplified probe beam and the conjugate beams (P' and C). The dashed line in all traces of figure 4 corresponds to the arbitrary level of -117 dBm on our spectrum analyzer. The annotated noise in each trace corresponds to the extra noise above the -117 dBm level at a noise frequency of 300 kHz. Figures 5b and 5c show the conjugate and amplified probe noise (respectively) versus noise frequency. Here (figures 5b and 5c) the noise is larger than a coherent beam of equal power (see figures 5e and 5f). Subtracting the conjugate and amplified probe signal greatly reduces the noise (see figure 5d). In fact, the subtracted noise signal is almost at the electronic noise level (see figure 5a). The unamplified probe noise (not shown) is smaller than the electronic noise. This demonstrates that the probe and conjugate are intensity noise correlated. Figures 5e, 5f, and 5g show that the backward and forward pump noises are uncorrelated. In particular, figure 5e is the noise in B; figure 5f is the noise in F; and figure 5g is the B-F signal which shows larger noise than in either F or B alone (expected for uncorrelated noise sources). For comparison, the F and B noise traces were made after attenuation of F and B to the same power levels of P and C. This shows the excess noise generated by the amplification process.

These observations, coupled with our theoretical calculations, provide indirect evidence of at least 10dB of quantum noise suppression. For direct observation of squeezing, it is necessary to suppress the classical noise to a level below the shot-noise limit. This can be achieved, for example, by reducing the classical noise in each pump by servo-stabilization of the laser intensities.

⁸ M.S. Shahriar and P.R. Hemmer, submitted to *Phys. Rev. A*.

⁹ O. Aytur and P. Kumar, *Phys. Rev. Lett.* 65: 1551 (1990).

In conclusion, we have demonstrated a high-gain, low-pump power medium that yields distortion-free propagation. Furthermore, there is a high degree of classical as well as quantum noise correlation between the amplified probe signal and the conju-

gate signal. Quantum noise suppression achieved this way may be useful in sub-shot-noise imaging applications such as parallel processors in optical computers.

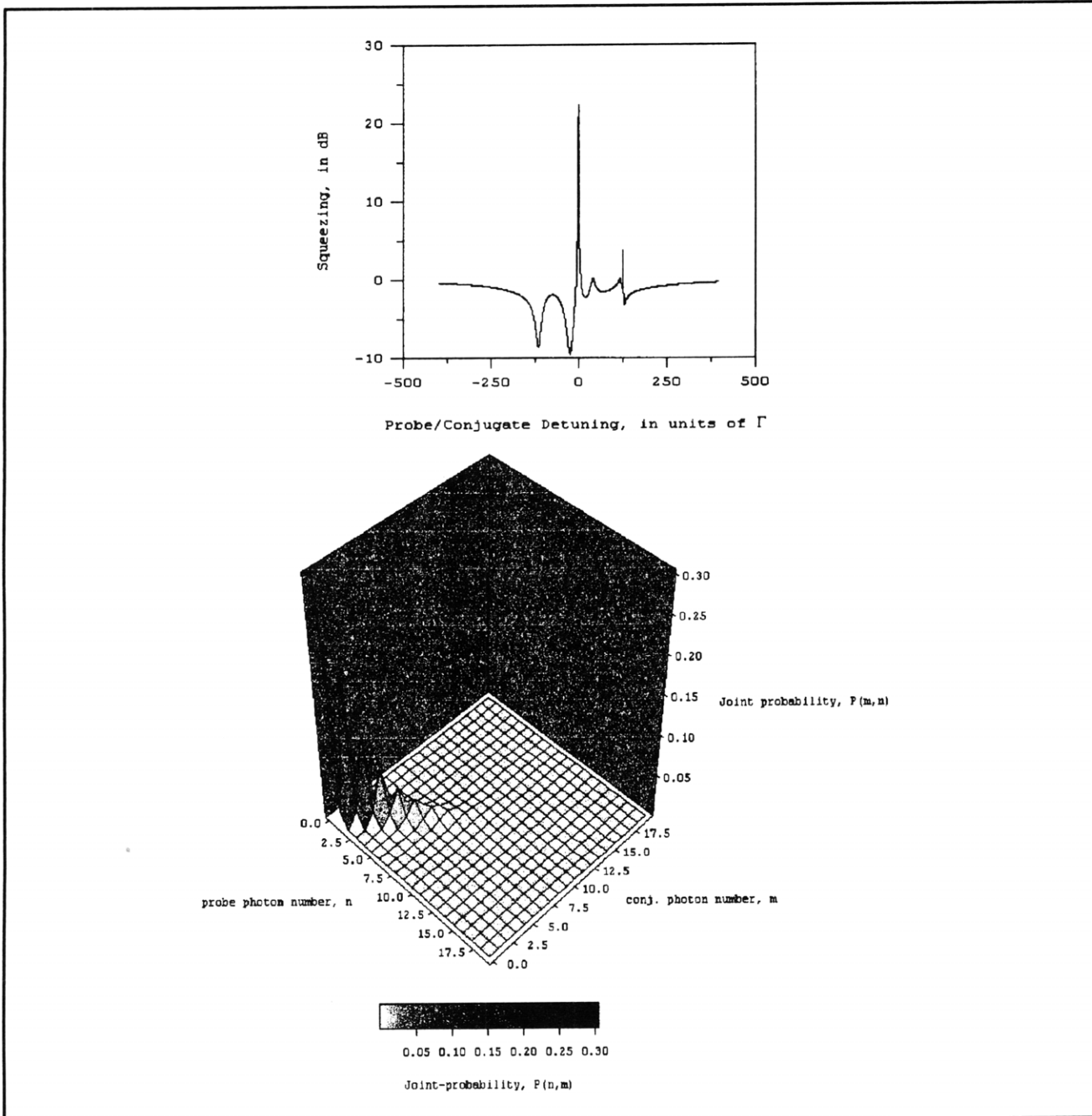


Figure 4. Theoretical predictions of quantum noise squeezing: (a) Quadrature squeezing, as a function of probe or conjugate detuning; and (b) the joint photon probability distribution for 10 dB twin beam squeezing, corresponding to the condition for maximum quadrature squeezing.

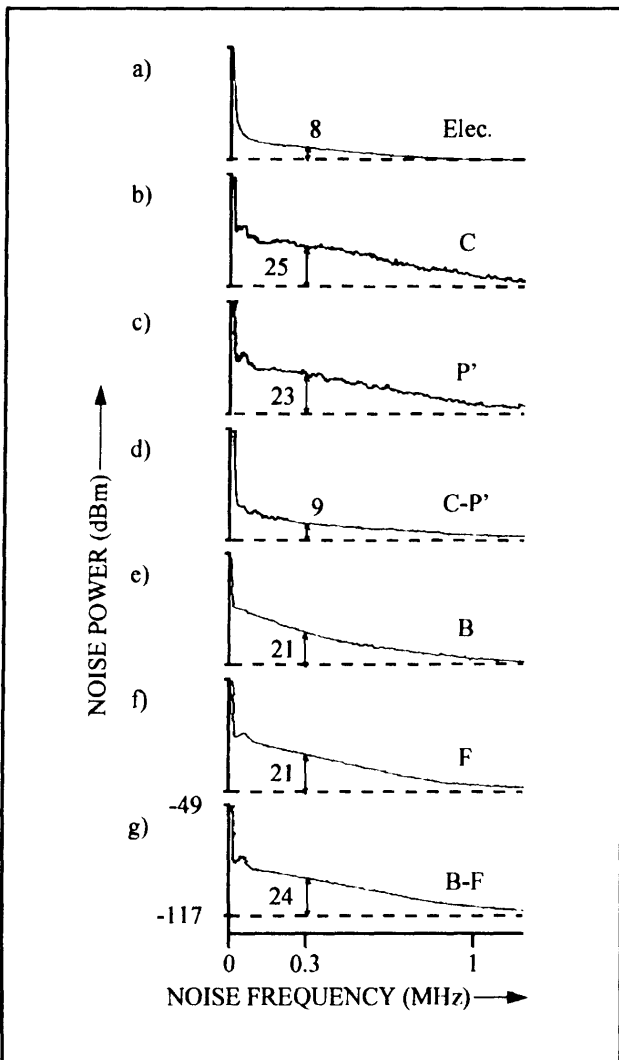


Figure 5. Noise versus frequency for a variety of conditions. The background noise level is marked with a dotted line (-117 dBm), and the noise at 300 kHz is tracked throughout. (a) Electronic noise of a pair of crossed photodiodes (the current produced in one photodiode opposes the current produced in the other). (b) The conjugate noise (one photodiode blocked). (c) The amplified probe noise (one photodiode blocked). (d) Subtraction of the conjugate and the amplified probe. Note that the noise is nearly equivalent to the electronic noise level. (e) Backward noise after it emerges from the four-wave mixer and attenuated to the power of the conjugate (one photodiode blocked). (f) Forward noise after it emerges from the four-wave mixer and attenuated to the power of the amplified probe (one photodiode blocked). (g) Subtraction of the backward and forward beams. Note that there is no noise reduction indicating that the backward and forward beam are not phase correlated.

1.2 Unbounded Cooling Force in Traveling Waves Excitation of a Four-Level System

Sponsor

U.S. Navy - Office of Naval Research
Grant N0014-91-J-1808

We have found a novel type of cooling mechanism using traveling wave excitation of a four-level system. This process yields cooling forces much larger than the spontaneous force, without intensity gradients. The force scales linearly with the Rabi frequency, as long as the laser detunings are also varied proportionately, and may be of use in open system (molecular) cooling. Unlike stimulated mechanisms of cooling, this process does not suffer from Doppleron resonances that heat other atoms while cooling only one velocity group.

In a two-level system under traveling wave excitation, the cooling force is bounded by the spontaneous force, given by the product of the photon momentum and the excited state decay rate. This is because the force in such a scheme originates from absorption of directed photons followed by emission of spontaneous photons in random directions. In the case of a standing wave excitation, this limit no longer holds. The atoms can in principle absorb photons from one direction, while emitting coherent photons in the other direction via stimulated emission. This process, known as stimulated cooling, requires symmetry breaking, leading to effects such as Doppleron cooling, which occur for specific combinations of velocities, Rabi frequencies, and detunings.¹⁰ For small variations in velocity, for example, the force can turn from heating to cooling. As a result, the standing wave cooling is not convenient for slowing down a thermal beam with a broad velocity spread.

It is generally held that the stimulated cooling requires the presence of intensity gradients. However, we have found a system where the stimulated redistribution of photons can occur even without the presence of any intensity gradients. Specifically, this scheme employs a four-level system, with two ground and two excited levels (the double Λ system). We find that the cooling force obeys very simple resonance conditions, and does not change sign over a large range of velocities. Moreover, this force scales linearly with the Rabi frequency, without bound (in the limit of rotating wave and electric dipole approximations). There-

¹⁰ M.G. Prentiss and A. Cable, *Phys. Rev. Lett.* 62: 1354 (1989).

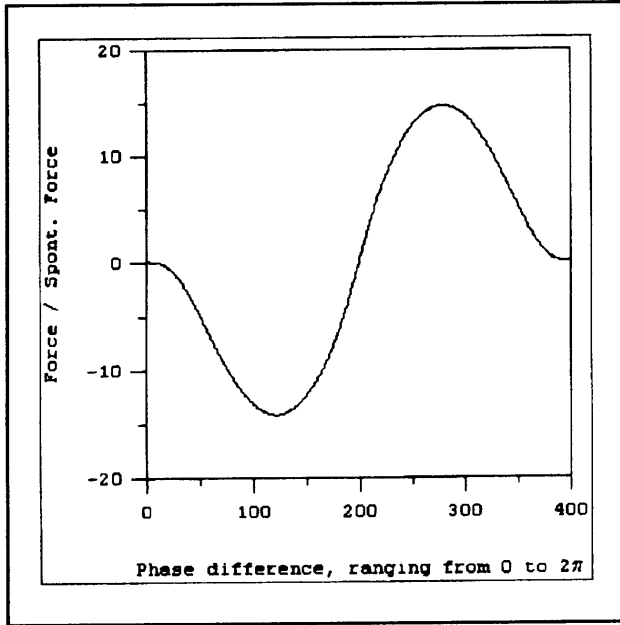


Figure 6. The resonant cooling force as a function of the closed loop phase, ϕ .

fore, this process may be used to provide very strong cooling over a short period of time and over a broad range of velocities. These properties makes this scheme a very attractive candidate for cooling open systems such as molecules.

Figure 1 shows schematically the level structure and the fields. Here, the fields F and P are traveling waves, propagating in the z direction, while B and C are traveling waves propagating in the opposite direction. The fields are assumed to have each the same Rabi frequency, g , and can be detuned independently, with the constraint (the so-called closed loop condition) that the two-photon detuning, Δ , (of F and P) matches the same for B and C. In addition, we limit ourselves to the condition that the average detuning, δ , of F and P is one-third that of B and C. One other parameter of interest is the (time independent) phase difference between the beat of F and P and that of B and C, denoted by ϕ . We find that when $\Delta=0$, $g=4\delta$, and $\phi = \pi/2$, the force is much larger than the spontaneous force, as illustrated in figure 6. Note that the force varies sinusoidally with ϕ . Moreover, if the Rabi frequencies and detunings are scanned while maintaining this ratio, the peak force scales linearly with the Rabi frequency, as shown in figure 7.

Briefly, this force results from a properly phased, symmetry-broken cycling of the atoms through the closed loop, with consecutive absorptions and stimulated emissions. Note that this force is fundamentally different from force rectification studied earlier under standing wave excitations of two¹¹ or three¹² level atoms. The rectified forces were only valid for zero velocity atoms, and are useful primarily for deflection. In contrast, the force considered here can be useful in deflection as well as cooling. For the later, one would have to chirp the frequencies and the intensities simultaneously, thus slowing down atoms, starting from the high velocity group, and sweeping all the atoms to a low velocity, much like the Zeeman slower, but much faster.

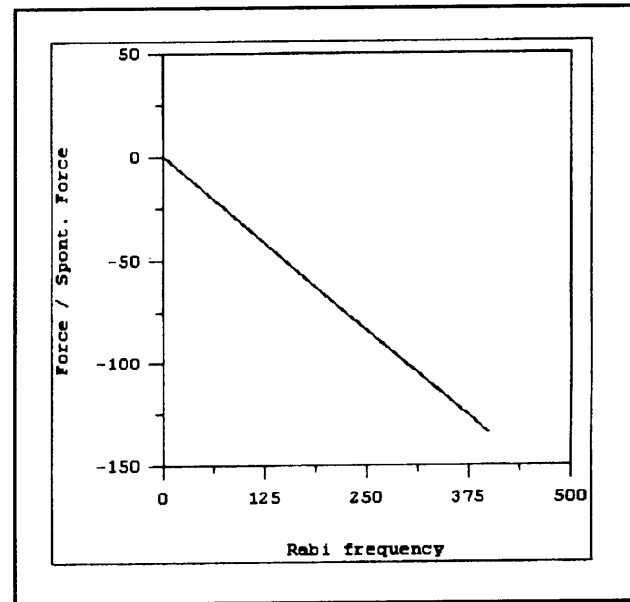


Figure 7. The maximum resonant cooling force for $\phi = \pi/2$, as a function of Rabi frequency, while the resonance condition is maintained.

1.3 Evidence of Collective Atomic Recoil Lasing in a High-Density Sodium Atomic Beam

We have observed that as atomic density is increased, strongly driven sodium atoms in a Doppler broadened system exhibit simultaneous gain and grating formation in the presence of a strong probe beam. This grating is properly oriented to deflect light from the pump into the probe, and is strong enough to significantly influence the

11 R. Grimm, Y.B. Ovchinnikov, A.I. Sidorov, and V.S. Letokhov, *Phys. Rev. Lett.* 65: 1415 (1990).

12 P.R. Hemmer, M.S. Shahriar, M.G. Prentiss, D.P. Katz, K. Berggren, J. Mervis, and N.P. Bigelow, *Phys. Rev. Lett.* 68: 3148 (1992).

probe gain. This positive feedback between the probe gain and the grating formation leads to exponential growth of the probe for a density exceeding a critical value. This observation is an apparent evidence of collective atomic recoil lasing (CARL),¹³ a process which may lead to coherent X-ray generation from relativistic particle beams using a low frequency pump.

Applications such as coherent X-rays generation from relativistic particle beams require the efficient direction reversal of coherent radiation. Currently, this is accomplished by back-diffraction from relatively weak bunched-particle gratings. However, it has been suggested¹³ that the efficiency of such gratings can be greatly enhanced by using internal states of the particles. Specifically, the CARL process proposes using the optical forces generated by the pump and probe beams to enhance bunching and therefore diffraction efficiency, which in turn amplifies the probe, creating positive feedback. Here, we show that efficient atomic gratings are formed in Doppler broadened sodium when a pump and relatively strong probe are present, and that at high atomic densities, these gratings can have a significant effect on the observed gain.

The experimental setup for observing the grating and its effect on the gain is shown schematically in figure 8. The Doppler broadened sodium source is an uncollimated atomic beam, excited immediately at the output of a 5 mm diameter effusive multi-collimator. This multi-collimator consists of a length of ridged nickel foil, rolled into a circular shape. The average channel is about $50 \mu\text{m} \times 250 \mu\text{m}$ with a length of 1.3 cm. At the oven temperatures used (from 300°C to 500°C), the mean free path of sodium is generally longer than the channel width, but shorter than its length. Under these conditions, the atom density in the beam is a fixed fraction of that in the oven, but the beam transverse velocity distribution is significantly broadened, compared to an ideal effusive multi-collimator.¹⁴ The measured Doppler width of the beam (at low oven temperature) is about 1.0 GHz, which is to be compared with the 1.5 GHz Doppler width of sodium vapor. The atomic density in the beam is estimated at about 110 times smaller than that in the oven,

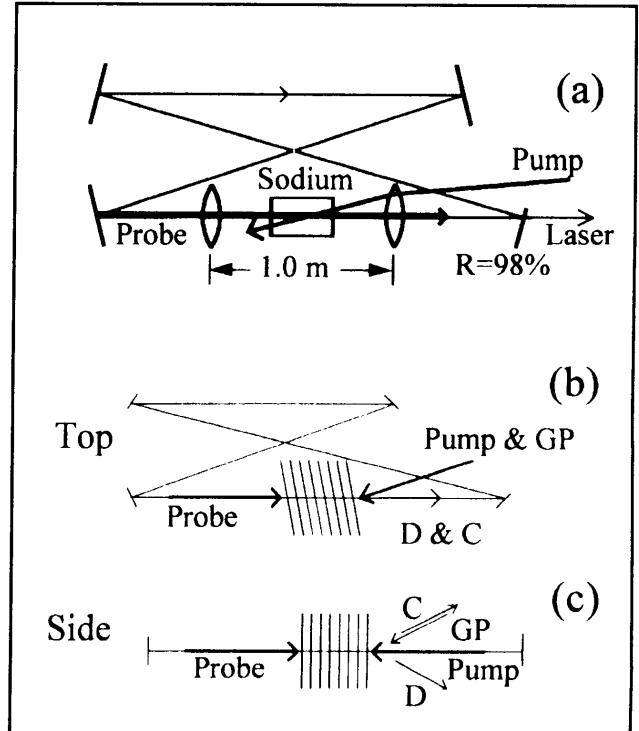


Figure 8. Schematic of experimental setup. (a) Setup for generating a strong back-propagating probe beam using a ring laser. (b) and (c) Top and side view, respectively, of setup for measuring grating diffraction efficiency.

based on geometric considerations and low temperature absorption measurements. The back-propagating probe beam is either supplied by a separate dye laser or else is generated by a back-propagating oscillation in a ring resonator which uses the sodium as an active medium.¹⁵ This second case is shown in figure 8a. Both pump and probe are focused to about 0.3 mm (FWHM) at the interaction region, using two 50 cm focal length lenses. The pump and probe are aligned about 10 mrad away from exactly counter-propagating for experimental convenience. Pump beam intensities range from 100 W/cm^2 to 1000 W/cm^2 , while the (intra-cavity) probe beam is up to 12 percent as intense as the pump. Typically, the pump is circularly polarized and is resonant with the sodium D_2 line.

¹³ R. Bonifacio, L. DeSalvo, L. M. Narducci, and E.J. D'Angelo, "Exponential Gain and Self-bunching in a Collective Atomic Recoil Laser," *Phys. Rev. A* 50: 1716-24 (1994).

¹⁴ H. Pauly, "Other Low-energy Beam Sources," in *Atomic and Molecular Beam Methods*, Vol. 1, Ed. G. Scoles (New York: Oxford University Press, 1988) pp. 83-123.

¹⁵ J.S. Kane, P.R. Hemmer, J. Donoghue, and M. Cronin-Golomb, "Bidirectional Oscillation and Phase Conjugation in a Sodium-vapor Ring Resonator," in *Quantum Electronics and Laser Science Conference*, 1992 OSA Technical Digest Series, Vol. 13 (Washington, DC: Optical Society of America, 1992) pp. 272-3; P.R. Hemmer, D.P. Katz, N.P. Bigelow, M.S. Shahriar, R. Bonifacio, and L. DeSalvo, *Phys. Rev. Lett.*, forthcoming.

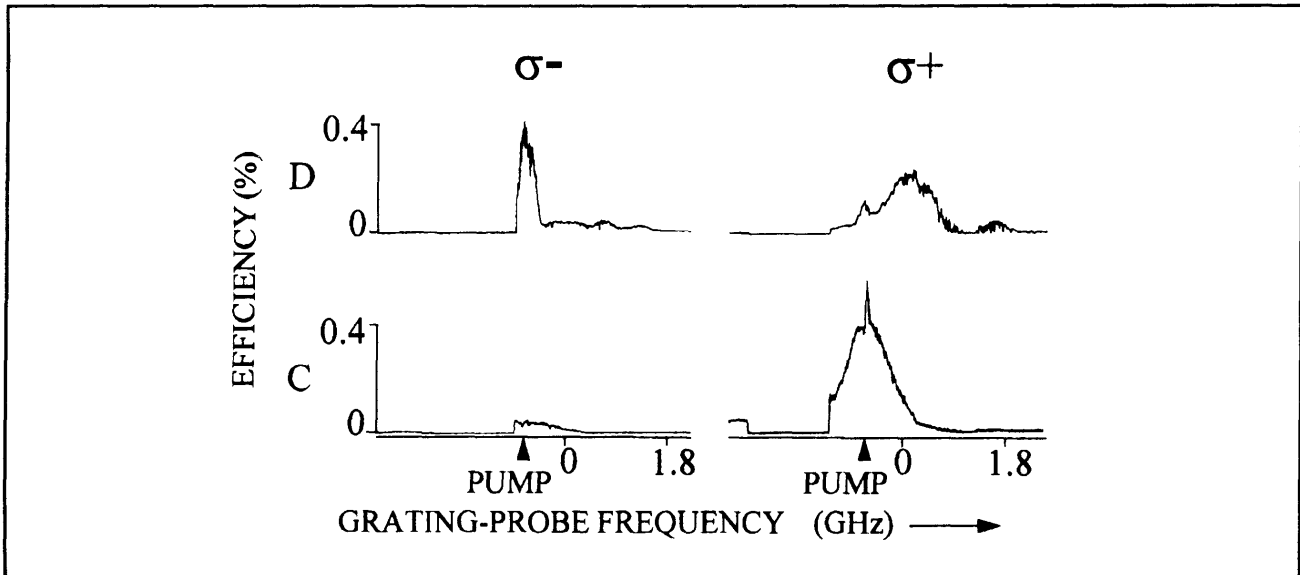


Figure 9. Grating diffraction (denoted by D) and conjugate (denoted by C) efficiencies versus grating-probe frequency. Here, σ^+ denotes a grating-probe with (circular) polarization identical to that of the pump, and σ^- denotes the orthogonal grating-probe polarization. The efficiencies are referenced to the grating-probe input power.

To observe the grating, an additional laser beam, called the grating-probe, is also focused into the interaction region, as shown in figure 8b and 8c. This grating-probe beam is typically from 4 percent to 25 percent as intense as the pump and is incident at an angle of about 10 mrad out of the pump/probe plane, but is approximately co-propagating with the pump when projected into this plane. The backscattered (or diffracted) portion of the grating-probe beam exits the interaction region in the same out-of-plane direction as the grating-probe, but the same in-plane direction as the back-propagating probe, as shown. Under some conditions, a phase conjugate beam is also observed, which is exactly counter-propagating with the grating-probe beam in all planes.

Typical diffraction and conjugate efficiencies as a function of grating-probe frequency and polarization are shown in figure 9. Here, the pump and back-propagating (intra-cavity) probe frequencies are held fixed. To accomplish this, the grating-probe is derived from an independent dye laser. The column labeled σ^+ in the figure denotes a (circular) grating-probe polarization which is identical to that of the pump, whereas σ^- denotes the orthogonal grating-probe polarization. As shown, in the case of a σ^- grating-probe, a diffracted beam is observed when the grating-probe is tuned to within 250 MHz (FWHM) of the pump frequency. For comparison, the calculated pump Rabi frequency is about 1.5 GHz, which is based on an input pump intensity of 280 W/cm² and the matrix elements for the $F = 2, m_F = 2 \leftrightarrow F = 3, m_F = 3$ sodium transition. For the data in figure 9, the (intra-cavity)

back-propagating probe intensity is about 0.8 W/cm² (or 0.3 percent of the pump), the grating-probe intensity is 10 W/cm², and the peak diffracted beam intensity is about 40 mW/cm² (or 0.4 percent of the grating-probe).

At peak diffraction efficiency, the intra-cavity, back-propagating probe is observed to be a factor of 2 weaker (not shown), which signifies a reduction in gain. To determine whether this gain reduction is due to perturbation of the grating or optical pumping, the experiment is repeated with the grating-probe tuned to the sodium D₁ transition, but all other conditions identical. Since the D₁ transition is 0.5 THz away from the D₂ transition, the grating-probe will no longer be Bragg matched to diffract from the grating. However, the optical pumping rate out of the $F=2, m_F=2$ ground state sublevel is about 2 times faster for σ^- excitation on D₁, compared to D₂, so that optical pumping effects are enhanced. When the grating-probe is tuned to be resonant with the same velocity group as the pump beam (which is analogous to peak diffraction condition in figure 9, σ^- case), no diffracted beam or intra-cavity probe attenuation are observed.

For identically (σ^+) polarized grating-probe and pump beams, a conjugate is observed when the grating-probe frequency is within 800 MHz (FWHM) of the pump frequency, as shown in figure 9. Diffraction is also observed, but its peak is a factor of 2 smaller than in the σ^- case and corresponds to a blue-shifted grating-probe. Attenuation of the back-propagating intra-cavity probe is also less (about 30 percent at peak diffraction). The 800 MHz linewidth of conjugate (and diffraction) efficien-

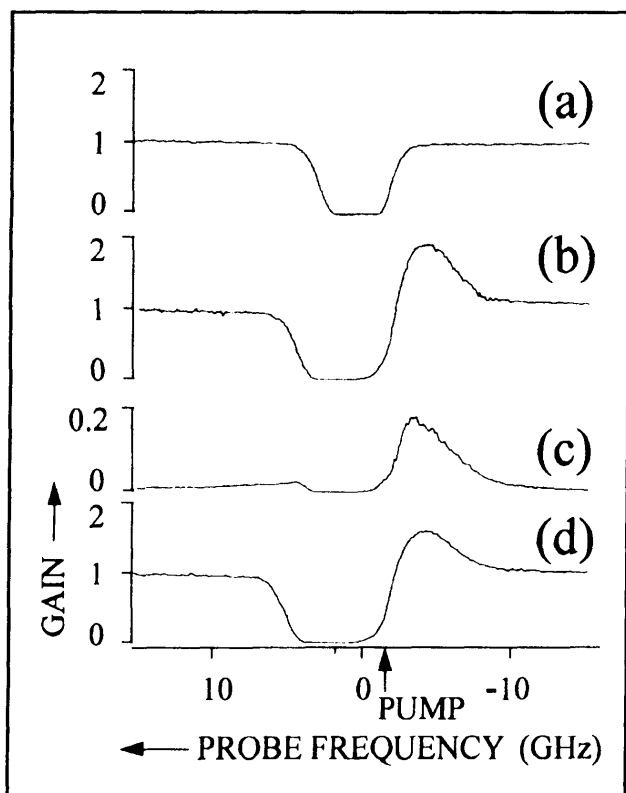


Figure 10. Gain versus back-propagating probe frequency. (a) Probe absorption in the absence of pump beams. (b) and (d) Probe gain spectrum in the absence and presence of a grating-probe, respectively. (c) Diffracted beam corresponding to (d).

cies in the σ^+ case is about 3.2 times the diffraction efficiency linewidth in the σ^- case. The reason for this is not clear. However, it is interesting to note that the ratio of summed optical transition probabilities for σ^+ versus σ^- transitions, starting from the $F=2$, $m_F=2$ sodium ground sublevel, is 3:1. Finally, the narrow spike in conjugate efficiency occurs when the pump and grating-probe frequency separation is comparable to the two-laser beat linewidth.

Figure 10 shows more clearly, the competition between gain and grating-probe diffraction. Here, figure 10a shows the probe absorption in the absence of a pump, figure 10b and 10d show the probe gain spectrum without and with the grating-probe, respectively, and figure 10c shows the diffraction efficiency. Clearly, the gain is reduced when light is diffracted from the grating. Moreover, the loss in output probe power is approximately equal to the power in the diffracted beam. For this

data, the ring cavity is blocked and the back-propagating probe beam derived from a second dye laser, which allows the probe frequency to be independently scanned. The grating-probe is derived from the same dye laser as the pump, but is orthogonally (σ^-) polarized. In order to achieve a high signal to noise ratio for this data, the gain is increased by increasing the pump intensity. Since the maximum dye laser output power is 300 mW, this is accomplished by replacing the 50 cm lenses by 30 cm lenses, separated by 60 cm. This reduces the pump (and probe) spot sizes to about 0.18 mm. The pump intensity is 800 W/cm², the probe intensity is 15 W/cm², and the grating-probe is 200 W/cm². Finally, with the shorter focal length lenses, it is found that the grating-probe and diffracted beams must be less than 5 mrad away from colinear to achieve high efficiencies.

Other measurements made on the diffracted beam include frequency, polarization, response time, and sensitivity probe beam propagation direction. When the grating-probe is derived from the pump beams, and therefore has exactly the same frequency, the diffracted beam is at the frequency as the probe. This is also true when the probe is generated by laser oscillation, except that in this case they both have the same spectrum, since the lasing is multi-mode. The rise time of the diffracted beam (when the back-propagating probe is chopped) is less than 20 nsec, the measurement being limited by the acousto-optic shutter response time. A grating is also observed when the back-propagating probe is replaced by a forward-propagating one. Moreover, diffracting off this forward-scattering grating reduces the forward probe gain, in analogy with the back-propagating probe case. However, forward-propagating probe, measurements are complicated by forward-scattering and self-defocusing of the pump beam, and will not be discussed further.

The competition between gain and grating-probe diffraction is very sensitive to atomic density. This is shown graphically in figure 11. Here, figure 11b shows the back-propagating probe gain as a function of atomic density, with and without the grating-probe present. Figure 11a shows the diffracted beam power, referenced to the input probe power. For these plots, the atomic density in the interaction region is estimated by dividing the calculated oven density (at each temperature) by the factor of 110 discussed earlier. Clearly, as atomic density is increased, the grating can have a significant effect on the gain.

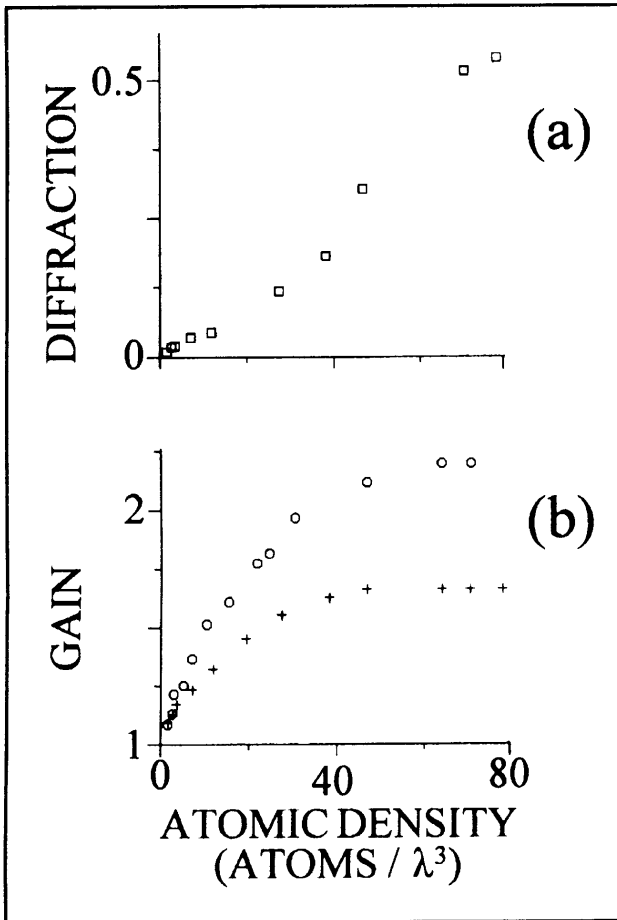


Figure 11. Peak gain and diffraction efficiency versus atomic density (units of atoms/ λ^3). (a) Diffraction efficiency in units of input back-propagating probe power. (b) Back-propagating probe gain in the absence (circles) and presence (+'s) of a grating-probe beam.

In summary, we have shown that efficient gratings can be formed in high density sodium in the presence of a pump and a strong probe. We also show that this grating can significantly influence the probe gain. This interdependence of gain and gratings is one of the necessary conditions for effects such as CARL. Finally, it is interesting to note that the atomic density for which this interdependence becomes significant is about 40 atoms/ λ^3 . This is close to the CARL threshold density of 100 atoms/ λ^3 , which is calculated by equating the CARL bandwidth¹³ of the relevant sodium transition to the measured inhomogeneous linewidth.

1.4 Applications of Porous Glass Based Thick Holograms for Optical Data Storage and WDM Demultiplexing

Sponsor

Ballistic Missile Defense Organization
Grant NG0921-94-C-0101

We have observed ultra-high Bragg selectivity in a new type of thick hologram, made using a novel material called Photopolymer with Diffusion Amplification (PDA). This material is very stable against temperature variation and does not suffer from differential shrinkage during development. As a result, holograms can be made as thick as 1 cm, which is nearly two orders of magnitude thicker than the thickest photopolymer based holograms currently in use. This opens up the possibility of using these holograms for enhancing the volume holographic data storage density by at least one order of magnitude. In addition, we can use a stack of these holograms to build an individual channel tunable demultiplexer for a wavelength division multiplexing (WDM) network.

Dynamic holograms, commonly known as phase conjugators, have flourished in many areas such as image processing, photon echo data storage, rectification of wavefront distortion, stable laser cavity designs, and so on. Static holograms, in comparison, have been somewhat limited in applications. One reason for this limitation is that it is difficult to produce thick static holograms. Consider, for example, a hologram made of dichromated gelatins. Typically, the gelatin is first deposited on a substrate of glass, followed by exposure to the image and write beams. During the post-exposure processing, the gelatin suffers from nonuniform shrinkage, which limits hologram thickness to no more than 100 microns. Recently, we, in collaboration with a company (Northeast Photosciences, Hollis, NH) and a group of scientists in Russia, have developed technologies to circumvent this problem, and have been able to produce inexpensive holograms that are a few millimeters thick, with a very high degree of Bragg selectivity.¹⁶

The advantages of thick holograms are numerous.¹⁷ For example, they possess high diffraction efficiency, they allow reconstruction of holograms from a fragment of a whole hologram (associative memory), and they are characterized by high

¹⁶ J.E. Ludman, J.R. Riccobono, H.J. Caulfield, J.M. Fournier, I.V. Semenova, N.O. Reinhand, P.R. Hemmer, and S.M. Shahriar, in *Proceedings of IS and T Conference*, San Jose, California, February 1995.

¹⁷ H. Kogelnik, *Bell Syst. Tech. J.* 48: 2909 (1969).

angular and spectral selectivity, which allow for recording multiple holograms at the same location. As such, these holograms are useful for enhancement of holographic storage density. Holograms with a thickness of 100 μm are currently used in commercially available volume holographic optical storage units.¹⁸ A 1 cm thick hologram will enhance the storage density of this proven technology by as much as two orders of magnitude.

Another very important application of thick holograms is in the development of individual channel tunable filters for a WDM network. Wavelength division demultiplexers are key elements in planned all-optical terabit computer networks linking supercomputers. Next generation wavelength multiplexers are expected to consist of laser arrays of up to 10 elements with precise 2 nm wavelength increments. The multiplexing operation is currently performed by waveguide combiners, even though these are somewhat lossy, because they are tolerant to wavelength errors. Demultiplexing is currently performed by curved diffraction gratings which can be fabricated either mechanically or holographically (thin holograms). Although adequate wavelength selectivity can be achieved with such devices, they are not tolerant to offsets or drifts in the operating wavelengths of the laser sources. While it is possible to compensate for wavelength errors common to all lasers in an array by temperature tuning, channel to channel offsets cannot be easily compensated for in curved grating structures. However, manufacturing tolerances or thermal crosstalk can result in channel to channel drifts on the order of 1 nm or more in a large, ten-element array. Thermal crosstalk is a potentially more serious problem since it occurs in real time, in response to individual lasers being turned on and off. Clearly, a device which is capable of compensating for channel to channel wavelength errors in real time while still maintaining high efficiency and the necessary frequency selectivity would be ideal for both multiplexing and demultiplexing operations.

It is well known that thick holograms can have sub-nanometer wavelength selectivity.¹⁹ For example, at a design wavelength of 1.5 μm a 2 mm thick hologram has a wavelength selectivity of better than 1 nm (Much more precise selectivity can be achieved using near-backward reflection geometry; however, 1 nm selectivity is typically warranted for WDM applications in order to allow signal modulation). The problem arises when it is desired to

simultaneously diffract more than one wavelength. Because of Bragg selectivity, multiple beam diffraction requires multiple holograms. If multiple exposures of a single substrate are used to write the required holograms, the diffraction efficiency for each individual hologram decreases rapidly as more holograms are written. The solution is therefore to use multiple substrates. To simultaneously diffract multiple beams, the individual holographic substrates are stacked. Since thick holograms that are not Bragg matched have very small diffraction efficiency, the light passes through most of the stack with minimal losses and is diffracted with high efficiency from the Bragg matched hologram. Typical efficiencies of 2 mm thick, phase holograms are about 95 percent for light near 1.5 μm optical wavelength. In contrast, non-Bragg matched diffraction is theoretically less than 5 percent on the strongest side-mode, so that much of the expected loss is due to incidental causes such as scattering in the substrate or surface reflections (which can be controlled by anti-reflection coatings). Thus, even a stack of 10 holograms would be expected to have an overall efficiency of greater than 50 percent. Of course, for a very large number of holograms (greater than 10 or 20), the stack concept becomes less practical, due to low overall diffraction efficiency and large physical size. However, most near term WDM systems do not anticipate using more than 10 wavelengths (limited by the required bandwidth for each channel, and the bandwidth of the Erbium doped fiber amplifier) and hence the stack concept becomes very competitive.

The basic setup for wavelength demultiplexing using a stack of thick holograms is illustrated figure 12. As shown, the output from an optical fiber is collimated with a microlens and directed through the stack. In each case, the diffracted light is collected by a lens and focused onto a single element of a photodetector array. To allow real time adjustment of the Bragg angle, each hologram is mounted on a separate flexure mount with a piezoelectric actuator. A 2 mm sized mount with an inexpensive, commercially available actuator capable of 1 μm displacement is adequate to provide the maximum anticipated 1 mrad tilt angle. Since the piezoelectric element is charge driven, it consumes essentially no power in the steady state. This sample device, consisting of eight holograms, would have an overall physical length of less than 2 cm.

¹⁸ H. Yu, S. Li, and D. Psaltis, *J. Opt. Soc. Amer. A* 12: 1902 (1995).

¹⁹ F.H. Mok, *Opt. Lett.* 18: 915 (1993).

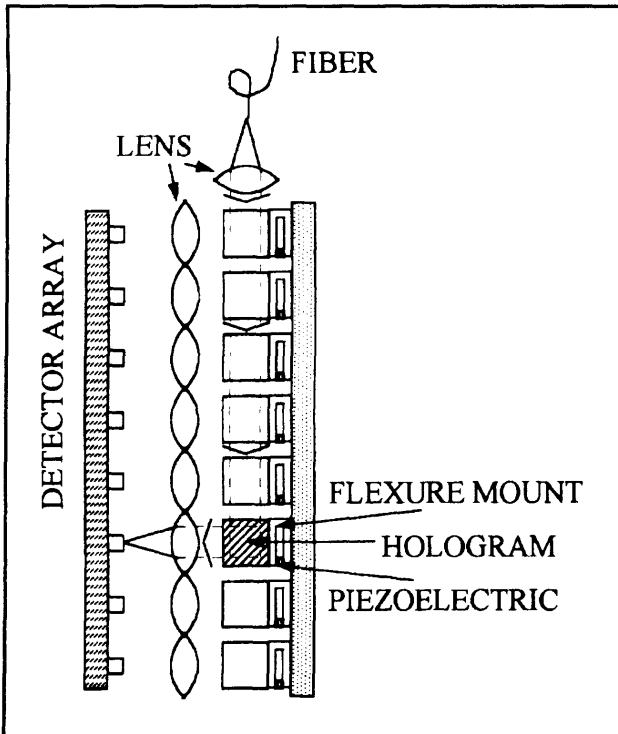


Figure 12. Schematic of an 8-wavelength fiber demultiplexer. Each wavelength is diffracted by only one hologram as illustrated.

With our collaborators in Russia, we have recently developed two novel materials for thick holographic data storage as well as WDM demultiplexing. These are (1) a thick porous glass substrate which can be embedded with a host of materials such as photopolymers or dichromated gelatin, and (2) a thick PolyMethylMethAcrylate (PMMA) based system called Photopolymer with Diffusion Amplification (PDA).

Consider first the porous glass system. A typical unit is a quartz porous glass matrix containing pores of about 10 to 30 nm in size. These pores are interconnected with a continuous network of capillaries. The photo-reactive materials (such as dichromated gelatin or a dye solution) can be introduced into the pores, aided by the strong capillary force (about 20 to 30 atm for 20 nm diameter capillaries). After the suspension liquid is dried off, the active molecules form a coating on the inner walls of the pores. The advantages of this substrate over amorphous polymer surface are numerous: (1) The porous glass is made of quartz, and can have a very high quality surface, and (2) The structure is very rigid, robust against thermal

stresses and fluctuations, and virtually immune to differential shrinkage. As a result, it should easily be possible to make high quality holograms as thick as 1 cm.

In collaboration with scientists from Russia, we have already demonstrated 1 and 2 mm thick holograms in porous glass, with dichromated gelatin as the embedded photo-reactive material. We have written plane wave fringes in order to use these holograms as nonspatial filters of laser noise. The observed Bragg selectivity and efficiency are consistent with the theory for thick holograms.¹⁷ While this material has the distinct advantage that it does not suffer from differential shrinkage during the post-exposure development of the holograms, there is room for further improvement in performance. For example, the density of pores in this glass are not uniform over the whole volume. This limits the quality of the output beam in applications such as Nonspatial Filtering. Recently, we have identified a new material, also developed by the same institute in Russia, that out-performs the porous glass in general, and solves the problem of nonuniformity in particular.²⁰

This material, known as PDA, consists of phenanthraquinone embedded in PMMA. This medium uses the novel principle of diffusion amplification of holograms on polymeric recording media. Briefly, photoexposure of this system results in writing of two out-of-phase periodic structures that partially compensate each other. One of these is formed by a concentration distribution of chromophore groups combined into macromolecules, while the other is formed by free molecules. As a result of diffusion of the free molecules, the corresponding grating degrades, and the resulting grating is amplified *without additional processing*. The surviving grating is stored in macromolecules that do not diffuse.

As stated above, the PDA thick holograms compare favorably with thick holograms made using porous glass. To start with, due to the immobility of the macromolecules that hold the final hologram, the PDA thick holograms are as robust as the porous glass ones. However, the PDA holograms do not suffer from any systematic variation in the concentration of the macromolecules. As a result, light diffracted from a plane wave PDA hologram shows a single Gaussian peak. In contrast, the density of pores in the porous glass is not uniform over the entire volume. Therefore, the diffracted spot in this

²⁰ A.V. Veniaminov, V.F. Goncharov, and A.P. Popov, *Opt. Spectrosc. (USSR)* 70: 505 (1991); A.V. Veniaminov et al., *Opt. Spectrosc. (USSR)* 60: 87(1991).

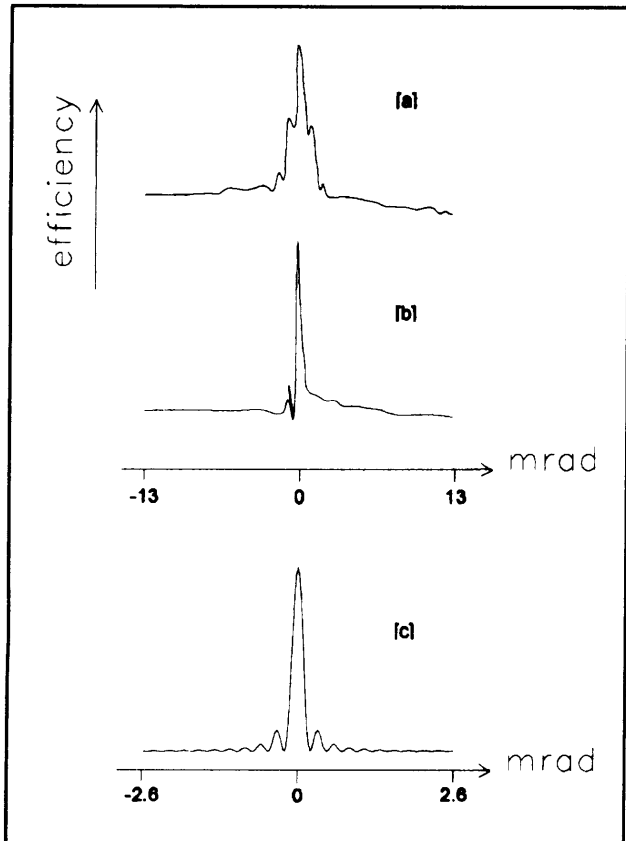


Figure 13. Experimentally observed angular selectivity of thick holograms, for (a) photopolymer embedded in porous glass (b) PDA. The theoretical plot (c) is for an ideal thick hologram, illuminated by a plane wave (note the difference in scale). When the Gaussian profiles and the corresponding divergence of the read and write beams are taken into account, the small sidelobes in (c) wash out, agreeing well with the output of PDA. The strong sidelobes in (b) represent the Fourier transform of the nonuniformity of pore densities. The sharp but small feature in (b) is an artifact, and the efficiency in each plot is normalized.

case shows additional sidebands, corresponding to the Fourier transform of the pore density nonuniformity. We have observed this distinction experimentally¹⁶ as illustrated in figure 13. As can be seen, the diffracted spot of the PDA thick hologram show a single peak (ignoring the experimental glitch), while the diffracted spot of the porous glass thick hologram has strong side-lobes. The observed Bragg selectivity of 1 mrad, along with the elimination of sidelobes, makes PDA very suitable for both thick holographic data storage and for WDM demultiplexing.

1.5 Distributed Fiberoptic Sensor for Quench Detection in Superconducting Tokamak Magnets

Sponsor

MIT Plasma Fusion Center

The next generation magnetic confinement fusion machines (tokamaks) will use superconducting, rather than conventional, magnets for confining and heating the plasmas. These magnets can be longer than a kilometer and typically are cooled using a forced flow of liquid helium through the conduit which surrounds the superconducting cable. The detection of a quench, i.e., a section of the magnet going normal, is very important since the local heating due to an undetected quench could lead to permanent magnet damage. Thus, a quick and reliable way of detecting such quenches is very important.

One novel method for detecting quenches in such a magnet is to include an optical fiber with the superconducting cable inside the conduit. Since the optical fiber is in close contact with the cable, any local heating of the cable also causes heating of the fiber, which can be detected interferometrically.

This technique has been successfully demonstrated in laboratory scale experiments²¹ and an experiment with a 100 meter cable is currently underway. This experiment, called ITER, is a part of an international scientific collaboration on fusion research between the United States, Japan, the European Union, and the Russian Federation. The test cable was made in Japan; the sensors were provided by the U.S.; and final preparations are underway for testing in Switzerland.

For this latest experiment, techniques had to be developed for embedding the fiber inside the superconducting cable and withstanding the numerous manufacturing steps required to build the sample, including a heat treatment with a temperature above 600° C for over 200 hours, and also cooling to 4 K during the experiment.

In order to survive the heat treatment, single mode optical fiber with a copper jacket instead of a conventional plastic jacket was selected. For additional mechanical protection, this fiber was covered with a

²¹ S. Pourrahimi, W.C. Guss, J.V. Minervini, D.B. Montgomery, N.T. Pierce, J.H. Schultz, S.P. Smith, and S. Ezekiel, "U.S. Contributions to the Development and Calibration of Quench Detectors for the ITER QUELL," *Proceedings of the Applied Superconductivity Conference*, Boston, Massachusetts, October 17-20, 1994.

glass braid and then encased in a stainless steel capillary tube.

Using this arrangement the optical fiber has survived the entire manufacturing process including sample cabling, insertion into the conduit, compaction, winding and heat treatment. Further, the fiber has now survived the cooling of the sample to liquid helium temperatures in preparation for testing.

1.6 Demonstration of an Optical Mass Flow Meter

Sponsor

MIT Plasma Fusion Center

The accurate measurement of liquid helium flow is important in a number of experiments and applications involving superconducting magnets. Conventional measurement techniques, such as venturis and orifice plates, have a number of drawbacks including a small dynamic range, constriction of the flow, poor bidirectional response, poor transient response and the need to measure several thermodynamic quantities to find the mass flow rate.

A new optical technique is being investigated for the measurement of the flow rate in an unseeded liquid helium flow. This technique has the advantages of a very large dynamic range, high accuracy, inherent bidirectionality, and virtually no constriction or disruption of the flow. In addition, the output of this sensor is proportional to the mass flow rate over a very wide range of thermodynamic conditions.²²

This flow measurement technique is based on the change in the speed of light in a moving medium, referred to as Fresnel drag. The relativistic calculation gives the speed of light in a moving medium, c_m , as,

$$c_m = \frac{c_0/n + v}{1 + v/nc_0} \approx \frac{c_0}{n} + \left(1 - \frac{1}{n^2}\right)v$$

where c_0 is the speed of light in vacuum, n is the index of refraction of the medium, and v is the velocity of the flow along the direction of light propagation. Thus, for a 1 m/s flow in liquid helium, the fractional optical path length change, $\Delta L/L$, resulting from this change in the speed of light is only about 2×10^{-10} .

One method of measuring this small effect uses a Sagnac interferometer, shown in figure 14.²³ Light from a source is coupled into a single mode optical fiber and is then split into two beams by a fiber coupler, C, and the beams are then sent in opposite directions around a fiber ring. The beams are then recombined using the same coupler C and the resulting intensity is measured using detector D. However, in contrast with either a Michelson or Mach-Zehnder interferometer, since both beams travel along the same path, any change in optical path length, for example due to fiber temperature changes or strain changes, is the same for both beams, i.e., the effect is reciprocal, and results in no change in the output intensity. Only effects which are nonreciprocal, i.e., different for the two directions of propagation, will result in a change in the output intensity.

Fresnel drag, as discussed above, is one such non-reciprocal effect. As shown schematically in figure 14, the light in the clockwise (CW) direction experiences a copropagating flow while the light in the counterclockwise (CCW) direction experiences a counterpropagating flow. Thus, the flow will cause a difference in the optical path length for the two beams, resulting in a phase shift between the two beams.

Figure 15 shows an initial demonstration of this flow meter using an unseeded water flow. For this experiment a 25 cm long flow cell was used with a maximum water flow velocity of about 27 cm/sec. As seen in the figure, this sensor detected both the magnitude and direction of the water flow. For comparison, the observed phase shift is equivalent to the phase shift expected for a 2.5 m/s flow of liquid helium in the same flow cell due to the much smaller index of refraction of liquid helium.

²² R.T. de Carvalho and J. Blake, "Slow-flow Measurements and Fluid Dynamics Analysis Using Fresnel Drag Effect," *Appl. Opt.* 33: 6073-6077 (1994); G.A. Sanders and S. Ezekiel, "Measurement of Fresnel Drag in Moving Media Using a Ring-Resonator Technique," *J. Opt. Soc. Am. B* 5: 674-678 (1988).

²³ J.L. Davis and S. Ezekiel, "Closed-loop, Low-noise Fiber-optic Rotation Sensor," *Opt. Lett.* 6: 505-508 (1981).

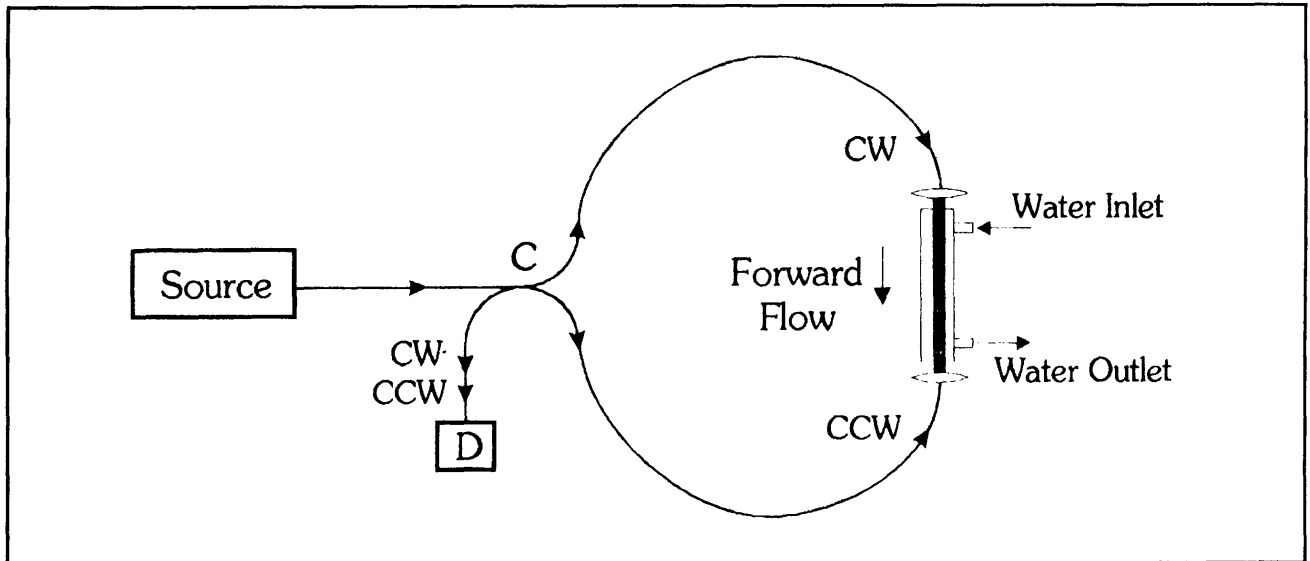


Figure 14.

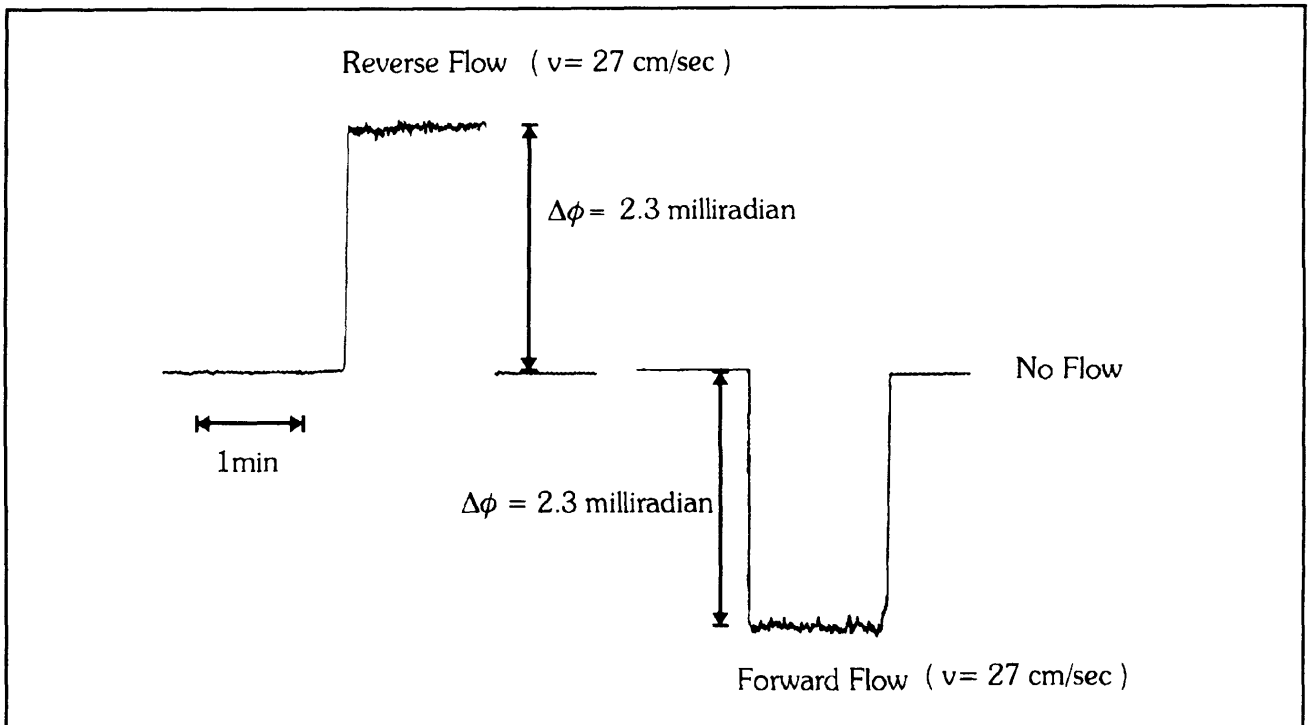


Figure 15.

An important feature of this flow meter is that the observed phase shift is not just proportional to the velocity of the flow, but, over a wide range of conditions, is proportional to the velocity of the medium times the density of the medium. Thus the sensor can be used to directly measure mass flow. The calculated mass flow rate sensitivity of this meter for a helium flow at a variety of pressures between

1 and 20 bars and a temperature range between 2 K and 1000 K only changes about ± 1 percent.

Thus, this sensor has the promise of yielding a mass flow output directly. In addition, it is inherently bidirectional, virtually immune to electromagnetic interference, insensitive to temperature and mechanical perturbations, as well as having a very high dynamic range and a very low sensitivity to magnetic fields.